Atmos. Meas. Tech. Discuss., 7, 5027–5073, 2014
www.atmos-meas-tech-discuss.net/7/5027/2014/
doi:10.5194/amtd-7-5027-2014

Atmospheric Measurement Techniques Discussions

Liquid water absorption and scattering effects in DOAS retrievals over oceans

E. Peters, F. Wittrock, A. Richter, L. M. A. Alvarado, V. V. Rozanov, and J. P. Burrows

Institute of Environmental Physics (IUP), University of Bremen, Otto-Hahn-Allee 1, 28359 Bremen, Germany

Received: 25 April 2014 – Accepted: 11 May 2014 – Published: 21 May 2014

Correspondence to: E. Peters (enno.peters@iup.physik.uni-bremen.de)

Published by Copernicus Publications on behalf of the European Geosciences Union.

Abstract

It is well-known that spectral effects of liquid water are present in absorption (DOAS) measurements above the ocean and insufficiently removed liquid water structures may interfere with trace gas absorptions leading to wrong (sometimes even non-physical) results. Currently available literature cross-sections of liquid water absorption are provided in coarser resolution than hyperspectral DOAS applications require and Vibrational Raman Scattering (VRS) is mostly unconsidered or compensated for using simulated pseudo cross-sections from radiative transfer modelling.

During the ship-based TransBrom campaign across the western Pacific in October 2009, MAX-DOAS measurements were performed into very clear natural waters achieving underwater light paths of up to 50 m. From these measurements, the retrieval of a residual (H_2O_{res}) spectrum is presented compensating simultaneously for insufficiencies of the liquid water absorption cross-section and broad-banded VRS structures. Small-banded (Ring) structures caused by VRS were found to be very efficiently compensated for by the intensity offset (straylight) correction included in the DOAS fit.

In the MAX-DOAS tropospheric NO_2 retrieval, this method was able to compensate entirely for all liquid water effects that decrease the fit quality. This was not achieved using a liquid water cross-section in combination with a simulated VRS spectrum. Typical values of improvement depend on the measurement's contamination with liquid water structures and range from ≈ 30 % for measurements slightly towards the water surface to several percent in small angles above the horizon. Furthermore, the H_2O_{res} spectrum was found to prevent misfits of NO_2 slant columns especially for very low NO_2 scenarios and thus increase the reliability of the fit. In test fits on OMI satellite data, the H_2O_{res} spectrum was found selectively above ocean surfaces where it leads to fit quality improvements of up to 6–18 %.

AMTD
7, 5027–5073, 2014

1 Introduction

In the atmosphere and ocean, liquid water interacts with solar radiation in the Visible in a variety of ways. Its absorption spectrum, which is called in the following H_2O_{liq} spectrum, results from vibrational transitions (overtone and combination bands) and is relatively smooth in shape (e.g., Pope and Fry, 1997). It causes the characteristic blue color of clear water. Suspended matter, so-called yellow substances, often dominates the water color, but this is not on focus of this study. In addition, inelastic scattering processes, both Vibrational Raman and Brillouin Scattering, by water molecules result in a change of the photon energy and thus change the spectrum of the incident light (Kattawar and Xu, 1992; Xu and Kattawar, 1994). Inelastic scattering produces a filling-in of Fraunhofer lines similar to the Ring effect in the atmosphere resulting form rotational Raman in-filling (Grainger and Ring, 1962).

In remote sensing observations of atmospheric trace gases in the Visible range over water surfaces, both liquid water absorption and in-filling of Fraunhofer lines are necessarily present and may disturb the trace gas retrieval if insufficiently compensated for. Obvious examples are satellite nadir measurements such as the GOME, SCIAMACHY, GOME-2, and OMI instruments (e.g., Burrows et al., 1995; Bovensmann et al., 1999; Callies et al., 2000; Levelt et al., 2006a, b). For example, the liquid water absorption in OMI measurements is shown in Fig. 1.

This study is concerned with the well-known remote sensing technique of Differential Optical Absorption Spectroscopy (DOAS) (e.g., Platt, 1994; Burrows et al., 2011). The DOAS method has been used for many years in order to detect atmospheric trace gases, e.g. NO_2, O_3, IO, BrO, HCHO, and CHOCHO from space (e.g., Burrows et al., 1999; Martin et al., 2002; Richter et al., 2005; Wittrock et al., 2006; Schönhardt et al., 2008; De Smedt et al., 2008) as well as from the ground, ships and aircrafts (e.g., Wittrock et al., 2004; Heckel et al., 2005; Peters et al., 2012; Pinardi et al., 2013; Großmann et al., 2013; Schönhardt et al., 2014).

AMTD
7, 5027–5073, 2014

Several previous studies demonstrated the presence of liquid water effects in satellite observations. Most of them were addressing the topic of Vibrational Raman Scattering (VRS). For example, Vountas et al. (2003) studied the impact of VRS on trace gas retrievals from the GOME satellite instrument and found that neglecting VRS can cause significant errors in the DOAS analysis, e.g. more than 30 % for BrO slant columns over clear ocean scenarios. In the UV, the filling-in of Fraunhofer lines by VRS in the ocean is decreased by chlorophyll and dissolved organic matter (DOM) as they absorb UV radiation. This was used to retrieve the oceanic chlorophyll content by Joiner et al. (2004). Different phytoplankton groups have been also successfully derived from SCIAMACHY satellite measurements using their absorption characteristics in an adapted (Phyto-)DOAS analysis (Vountas et al., 2007; Bracher et al., 2009). More recently, Rozanov et al. (2014) modelled the effect of inelastic Raman scattering in ocean water using the radiative transfer model SCIATRAN. With this, VRS was used in hyperspectral satellite data as a proxy for the abundance of light in the global ocean which is an important parameter for modelling phytoplankton primary production (Dinter et al., 2014). However, spectral effects of liquid water are not only present in satellite nadir observations, but also in ground-based MAX-DOAS measurements towards the water surface, close to the horizon and even at small elevation angles above the horizon as some photons observed under these viewing directions have traveled some distance within the water before being scattered into the line of sight. For example, Großmann et al. (2013) included a VRS spectrum to improve their MAX-DOAS fit of IO in the marine boundary layer over the remote ocean.

In small DOAS fitting windows, the smooth liquid water absorption spectrum is often assumed to be sufficiently compensated for by the DOAS polynomial. This is most likely the reason for the variety of studies on VRS while studies concerning the absorption structure are rare. However, for large fitting windows (> 40 nm in the Visible, depending on the actual fit settings and order of DOAS polynomial), liquid water absorption should be considered in the fit. For example, Richter et al. (2011) demonstrated that including the H_2O_{liq} spectrum in the GOME-2 DOAS fit for NO_2 (425–497 nm) improves

AMTD
7, 5027–5073, 2014

the fit quality. However, even in small fitting windows H_2O_{liq} can cause problems for the retrieval of weak absorptions if it is not compensated for. E.g., for CHOCHO which is mostly retrieved in the range of ≈ 435–460 nm, Lerot et al. (2010) have developed a two-step approach fixing the liquid water slant columns in the small glyoxal fitting window to results obtained in a larger fitting window where the smooth shape of the liquid water absorption spectrum can be retrieved more reliably.

Laboratory measurements of the pure liquid water absorption coefficient were performed for example by Pope and Fry (1997). Unfortunately, this absorption coefficient is given only in 2.5 nm steps and the spectral resolution is even lower (≈ 7 nm). Even though the absorption structure is smooth, the coarse resolution blurs the exact position of shoulders in the H_2O_{liq} spectrum. If the liquid water absorption is strong, this uncertainty can cause severe problems for the retrieval of trace gases using the DOAS method that requires spectral resolution in the range of < 1 nm. In addition, the liquid water absorption spectra as measured by different groups differ clearly from each other in the 400–500 nm range (e.g., see Dickey et al., 2011) which is a result of the weak absorption strength in the Visible (for short light paths, water appears to be transparent). As a consequence, very long light paths are needed to obtain reliable measurements. For the DOAS analysis, the 400–500 nm range is crucial as many trace gases (O_3, NO_2, CHOCHO, IO) are retrieved here. Furthermore, laboratory measurements of liquid water absorption were made using pure water under standard conditions (i.e. for fixed temperature and pressure). In contrast, the water absorption that is present in field or satellite measurements applies not to standard conditions and properties of real ocean water like salinity may have further influence on the absorption spectrum.

In this study, we report on MAX-DOAS observations pointing towards the water surface during the ship-borne TransBrom campaign in the western Pacific in 2009 where regions of remarkable clear water were encountered (see Fig. 1). These measurements were designed in a way that minimizes atmospheric contributions to the resulting optical depth while at the same time maximizing the liquid water influence. From these measurements, we retrieve a hyperspectral H_2O_{res} spectrum compensating simultaneously

AMTD
7, 5027–5073, 2014

for broad-banded VRS structures and uncertainties of currently available literature cross-sections of liquid water absorption. The influence and the potential improvement of the retrieved spectrum on the NO_2 fit using atmospheric MAX-DOAS measurements (i.e. close to and above the horizon) taken during the same campaign is investigated. In addition, the H_2O_{res} spectrum was tested and successfully found in complimentary satellite data.

The following Sect. 2 gives the theoretical background of liquid water spectral effects. Detailed information about the measurements performed as well as the DOAS method and the instrumentation is provided in Sect. 3. Section 4 reports about different attempts to retrieve experimental H_2O_{liq} and VRS cross-sections as well as the retrieval of the finally used H_2O_{res} spectrum. The influence of this spectrum on the NO_2 fit of atmospheric MAX-DOAS measurements is investigated in Sect. 5. Finally, the presence of the H_2O_{res} spectrum in OMI satellite data is demonstrated in Sect. 6.

2 Spectral effects of liquid water

The most important spectral feature of liquid water is its absorption H_2O_{liq}, which is different from the absorption spectrum of water vapour. Whereas the latter one is dominated by a large number of distinct vibrational-rotational absorption lines (caused by numerous rotational levels due to the H_2O molecule's different moments of inertia for rotation around different spatial axes), in the liquid phase, rotations are suppressed as a result of intermolecular hydrogen bonding and limited to so-called *librations* (rocking, wagging and twisting). Also, in contrast to most other substances, the absorption of liquid water in the visible range is not based on electronic transitions. Instead, it is caused by overtones of the three fundamental vibrational modes: symmetric stretch (ν_1), asymmetric stretch (ν_3) and bending or scissors mode (ν_2). The result is a continuous absorption spectrum that is smooth in shape with small values in the blue range and increasing values towards larger wavelengths. Thus, water absorbs stronger in the red part of the spectrum which produces the blue color of the ocean. The absorption

AMTD
7, 5027–5073, 2014

spectrum in the range focused on here is plotted in Fig. 2 (green line). The dominant stretch modes of the OH bond (ν_1, ν_3) occur at wavenumbers of $\approx 3400\,\mathrm{cm}^{-1}$ ($\approx 3\,\mu\mathrm{m}$) and the bend or scissors mode (ν_2) appears at $\approx 1600\,\mathrm{cm}^{-1}$ ($\approx 6\,\mu\mathrm{m}$) which is in the infrared region. The absorption in the Visible is caused by harmonics and linear combinations of these fundamental modes and strong transitions can be identified as shoulders in the absorption spectrum. For example, the shoulder at $\approx 450\,\mathrm{nm}$ corresponds to the seventh harmonic of the OH-stretch (see Pope and Fry, 1997, and references therein). Hydrogen bonds developing between adjacent H_2O molecules in the liquid phase decrease the vibrational energy levels of OH-stretches and thus cause a red-shift of vibrational transition energies (Braun and Smirnov, 1993, and references therein). With increasing temperature, hydrogen bonding decreases in importance, as a larger fraction of bonds is broken. As a result, the red-shift and therefore the exact position of absorption features (shoulders) is slightly temperature dependent (lower temperatures lead to larger red-shifts).

In atmospheric remote sensing, the effect of Rotational Raman Scattering (RRS) on air molecules (predominantly N_2) is well-known. RRS is an inelastic scattering process producing wavelength shifts of up to $50\,\mathrm{cm}^{-1}$ (Kattawar et al., 1981) corresponding to several Ångström ($10^{-10}\,\mathrm{m}$) in the Visible. As this is comparable to the width of strong Fraunhofer lines (and also in the range of typical instrumental resolution), more intensity is shifted from the wing of a Fraunhofer line into its core than from the core to the wing, simply because there is less intensity in the minimum that can be shifted. The result is a filling-in of Fraunhofer lines which was first observed by Grainger and Ring (1962) and is known as the Ring effect.

Similarly, also inelastic Vibrational Raman Scattering (VRS) can occur on molecules having vibrational modes, but the mechanism of filling-in of Fraunhofer lines (Ring effect) is less efficient and therefore VRS in the atmosphere can be neglected. In contrast, in liquid water the VRS effect on H_2O molecules becomes important because of the high density of water. At the same time, no RRS can occur in liquid water because no rotations are allowed as a result of intermolecular hydrogen bonding. The Ring effect

AMTD
7, 5027–5073, 2014

of VRS is somewhat different from RRS: The final energy E_{fin}, resp. wavelength λ_{fin}, of an inelastic VRS scattered photon is

$$E_{fin} = E_{int} - h \cdot c \cdot \tilde{\nu}$$
$$\Leftrightarrow \frac{1}{\lambda_{fin}} = \frac{1}{\lambda_{int}} - \tilde{\nu} \quad (1)$$

As the energy of the dominant OH-stretch is in the range of $\tilde{\nu} \approx 3400\,\mathrm{cm}^{-1}$ (see Fig. 3), for an initial wavelength λ_{int} of 400 nm Eq. (1) yields a final wavelength of ≈ 460 nm (for the Stokes-Raman-band), i.e. the VRS produces a wavelength shift of about 60 nm in the Visible. This maps larger structures of the initial sunlight spectrum to different positions. In addition, it is much larger than the wavelength shift due to RRS on N_2 molecules in the air and also much larger than the width of any Fraunhofer line. Consequently, the filling-in is predominantly not caused by more photons shifted from the line wing inside the core than vice versa. Moreover, the large line width of the VRS Raman band is responsible for the Ring effect. First, the line width is broad because of broadening effects in the liquid phase. In addition, the Raman band shape is a superposition of different Gauss curves, associated to monomers (single H_2O molecules) and polymers forming because of intermolecular hydrogen bonding. As this decreases the energy of the OH-stretch (as metioned above) the Raman band of polymers is centered at a different energy. For example, Walrafen (1967) and Kattawar and Xu (1992) described the Raman band as a superposition of 4 different Gauss curves (the resulting shape is plotted in Fig. 3). As the overall line width (≈ 8 nm in the visible) is much larger than any Fraunhofer line, the level of both the wing and the core are raised by roughly the same amount, i.e. the core is less deep relative to the wing after the VRS (Xu and Kattawar, 1994). As the number of hydrogen bonds is temperature-dependent, the shape of the Raman band is also temperature dependent. This has been used for remote sensing of the ocean temperature using LIDAR systems (e.g., Leonard et al., 1979).

AMTD
7, 5027–5073, 2014

To conclude, the resulting cross-section of VRS is both small-banded because of the filling-in of Fraunhofer lines as well as broad-banded because of the large intensity shift that maps larger structures of the initial sunlight spectrum. An example of the cross-section of VRS is given in Fig. 4. The prominent increase (step) around 460 nm results from the relatively sharp increase in intensity of the sunlight spectrum shortly before 400 nm (after the strong K and H Fraunhofer lines from Ca^+).

Another inelastic scattering effect is the so-called Brillouin Scattering that is caused by density fluctuations (phonons) in the water (e.g., Hickman et al., 1991; Dickey et al., 2011). In principle, Brillouin Scattering can also produce a filling-in of Fraunhofer structures, but the spectral shift is only several 10^{-3} nm in the visible range (Xu and Kattawar, 1994). This is much smaller than the shift of VRS or even RRS and also smaller than Fraunhofer lines that can be resovled with current (MAX-)DOAS instruments. Also the Brillouin linewidth in the Visible ($\approx 10^{-4}$ nm) is much smaller than for VRS (Xu and Kattawar, 1994). To conclude, the Ring effect caused by Brillouin Scattering can be neglected for current DOAS applications. Note, this was investigated in more detail in (Peters, 2013), but it is not reproduced here since the findings only confirmed the intuitive assumption above.

3 Measurements

3.1 The DOAS principle

The DOAS method (e.g., Platt, 1994; Platt and Stutz, 2008) is based on Lambert–Beer's law which is in its simplest form for the case of multiple absorbers

$$I(\lambda) = I_0(\lambda) \cdot e^{-\sum_i \sigma_i(\lambda) \cdot \rho_i \cdot s} \tag{2}$$

and describes the attenuation of light of initial spectrum $I_0(\lambda)$ through absorbers i of concentration ρ_i and absorption cross-section $\sigma_i(\lambda)$ along the light path s. However, in this equation ρ_i (and σ_i) must not depend on the light path. In first approximation, this

AMTD
7, 5027–5073, 2014

is true for the absorption of light under water because $\rho_{\text{water}} \approx \text{const}$. The product of ρ_{water} and liquid water absorption σ_{water} is of dimension m^{-1} and called the absorption coefficient. In contrast, the concentrations ρ_i of atmospheric absorbers have a vertical profile and thus vary strongly along the light path. This leads to the DOAS equation

$$\tau(\lambda) = -\sum_i \sigma_i'(\lambda) \cdot \text{SC}_i - \sum_p a_p \lambda^p + r(\lambda) \tag{3}$$

where $\tau(\lambda) = \ln\left(\frac{I(\lambda)}{I_0(\lambda)}\right)$ is the optical depth (I_0 is usually a sun spectrum for satellite- and a zenith spectrum for ground-based measurements), $r(\lambda)$ a residual spectrum and $\text{SC}_i = \int \rho_i(s)\text{d}s$ the so called slant column, which is the concentration of absorber i integrated along the light path. Note that the Ring effect explained above can be treated as additional absorber i and is included in the sum over absorbers in Eq. (3). For the atmospheric Ring effect due to RRS, a pseudo cross-section σ_{Ring} can be simulated using radiative transfer models like SCIATRAN (Vountas et al., 1998; Rozanov and Vountas, 2014) and as mentioned earlier, this is also possible for the VRS effect in liquid water (Rozanov et al., 2014).

The basic idea of the DOAS method is to separate the observed optical depth into a high frequency and a low frequency component. The low frequency component describes (1) possible instrumental effects and (2) smooth changes in the spectrum caused by Rayleigh (λ^{-4}-dependence) and Mie ($\lambda^{-\kappa}$-dependence, $\kappa = 0, \ldots, 2$) scattering. In addition, in satellite observations the low frequency component compensates also for the spectral surface reflectance. This low frequency component is accounted for by a polynomial of small order (usually 2nd to 4th order). The high frequency component consists of the high frequency parts $\sigma_i'(\lambda)$ (differential cross-sections) of absorber cross-sections $\sigma_i(\lambda)$. The DOAS equation is then solved by means of a least squares fit, i.e. the sum of squared residual points (chisquare) is minimized. The chisquare normalized by the number of spectral points is called RMS (root mean square) and a measure of the fit quality. The fit results are the coefficients of the polynomial (which are of no interest here) and the slant columns SC_i of the different trace gases. It is

AMTD
7, 5027–5073, 2014

important that the absorber cross-sections σ_i' included in the DOAS fit need to have different (and unique) structures, i.e. if one cross-section can be described by a linear combination of other cross-sections, the resulting slant columns are not meaningful.

3.2 Intensity offset correction (straylight correction)

In the context of this work, the method of accounting for intensity offsets superposing the measured spectrum is important. These intensity offsets can be caused by different effects, e.g. the detector's dark current. A prominent source of intensity offsets is straylight inside the spectrometer which is predominantly light reflected on any surface and finally reaching the CCD-detector at a position that does not correspond to its wavelength. An additive amount of light C (either real, i.e. straylight, or an instrumental artifact, i.e. dark current) influences the resulting optical depth $\tau(\lambda)$ as follows:

$$\begin{aligned}\tau(\lambda) &= \ln\left(\frac{I(\lambda)+C}{I_0(\lambda)}\right) = \ln\left(\frac{I(\lambda)}{I_0(\lambda)}\cdot\left[1+\frac{C}{I(\lambda)}\right]\right)\\ &= \ln\left(\frac{I(\lambda)}{I_0(\lambda)}\right)+\ln\left(1+\frac{C}{I(\lambda)}\right)\\ &\approx \ln\left(\frac{I(\lambda)}{I_0(\lambda)}\right)+\frac{C}{I(\lambda)}\end{aligned} \tag{4}$$

where the Taylor expansion for $\ln(1+x)$ was stopped after the term of first order. Consequently, the intensity offset causes a term of optical depth that is proportional to $1/I(\lambda)$.

In the DOAS analysis, this effect is routinely compensated for and called the intensity offset or *straylight* correction. Therefore, after a first guess for C, the additive $C/I(\lambda)$ term is used as an additional differential cross-section σ_{offset} in the DOAS fit (i.e. a corresponding slant column is fitted). As a consequence of the $1/I(\lambda)$-dependence, the differential cross-section σ_{offset} consists predominantly of Fraunhofer structures and

AMTD
7, 5027–5073, 2014

has therefore similarity to the Ring cross-section. This is intuitively clear: if a constant signal C superposes a spectrum $I(\lambda)$, then the relative contribution is largest where the original spectrum has lowest intensity, which is the case at the position of Fraunhofer lines.

Because of the similarity to the Ring spectrum, the intensity offset correction (i.e., σ_{offset}) was found to compensate very efficiently for the small-band structures of VRS. This has been already found in previous studies of (Vountas et al., 2003). Note that sometimes also higher intensity offset corrections (linear wavelength dependence etc.) are used, but for this study a constant straylight correction turned out to be sufficient.

3.3 Instruments

The focus of this study is on ground-based Multi-AXis (MAX)-DOAS measurements. In addition, OMI satellite data has been used in Sect. 6.

The IUP-Bremen MAX-DOAS instrument used here is a two-channel instrument consisting of two spectrometers for the UV and visible range, respectively, which are actively temperature stabilized at 35 °C. For this study, only measurements from the visible spectrometer are used, which is an Acton500 with a two-dimensional ROPER CCD camera with 100 × 1340 pixels covering a wavelength interval from 400–570 nm at a resolution of 0.8 nm. The spectrometers are connected via a 20 m long Y-shaped optical fibre bundle consisting of 2 × 38 = 76 single fibres (and thus overcoming polarization effects) to a telescope unit which collects sunlight. The telescope unit is mounted on a commercial ENEO VPT-501 Pan-Tilt-Head allowing pointing in any viewing direction. Light enters the telescope through a fused silica window and is focused by a lens on the optical fiber bundle entrance. The telescope's field of view (FOV) is $\approx 1.2^{\circ}$. Inside the telescope housing, a video camera for scene documentation (taking snapshots every 5 s) and a Mercury/Cadmium (HgCd) line lamp for calibration measurements are installed. All measurements and system operations are controlled by in-house software. The instrument demonstrated excellent performance during the intercomparison field

AMTD
7, 5027–5073, 2014

campaign CINDI a few months before TransBrom (Roscoe et al., 2010; Piters et al., 2012; Pinardi et al., 2013), where it was selected as one of the reference instruments.

The Ozone Monitoring Instrument (OMI) is a nadir-viewing imaging spectrometer on NASA's EOS Aura satellite launched on 15 July 2004 into a Sun-synchronous, polar orbit at approximately 705 km altitude. The local equator crossing time is between 13:40 and 13:50. OMI measures direct and atmosphere-backscattered sunlight in the UV-VIS range from 270 nm to 500 nm. Atmospheric observations are performed perpendicular to the flight direction in a 114° field of view corresponding to a 2600 km wide spatial swath on the Earth's surface. Due to the large field of view, the ground-pixel size varies across-track from 24 km (nadir) to 128 km (edge of the swath). Global coverage is achieved in one day. Further information about the OMI satellite instrument can be found in (Levelt et al., 2006a, b).

3.4 The TransBrom field campaign

TransBrom was a ship-borne field campaign across the western Pacific ocean. It was carried out onboard the German Research vessel *Sonne* starting at 9 October 2009 in Tomakomai, Japan (42°38′ N, 141°37′ E) and arriving at 24 October 2009 in Townsville, Australia (19°15′ S, 146°49′ E). A campaign overview can be found in (Quack, 2010) and (Krüger and Quack, 2012). The campaign's focus was on measurements of short-living halogen (in particular bromine) compounds in the sea as well as in the air and especially on the flux from sea to air, but this is not the topic of the present study. Furthermore, we already reported on the MAX-DOAS contributions and measurements of atmospheric trace gases (NO_2, HCHO, IO) during TransBrom (Peters et al., 2012; Großmann et al., 2013).

The cruise track is plotted in Fig. 1 together with the liquid water absorption slant columns retrieved from the OMI satellite instrument for August 2007 (these slant columns result from the OMI NO_2 fits (OMI-Fit2) as explained in Sect. 6). As the liquid water absorption coefficient from Pope and Fry (1997), which is of dimension m^{-1}, was used in that fit ($\rho_{water} \approx$ const, see Sect. 3.1), the resulting slant columns are of

AMTD
7, 5027–5073, 2014

dimension m and give the average length of the light paths that photons contributing to the respective measurement have been traveling under water. Obviously, the TransBrom cruise was carried out almost entirely in a region of very clear water where average underwater light paths of ≈ 7 m occur in measurements from the satellite. From the MAX-DOAS measurements being installed on the RV *Sonne* and pointing directly into the water, even longer light paths (up to 50 m) were achieved.

3.5 MAX-DOAS set-up and viewing geometry

During the TransBrom campaign, the MAX-DOAS telescope unit was installed at the monkey deck above the bridge of the RV *Sonne* pointing portside. For measurements of atmospheric trace gases, vertical scans in elevation angles ranging from −3° (slightly towards the water surface) to 30° above the horizon were performed in an azimuthal direction perpendicular to the ship (i.e. −90° relative to the ship's heading). These measurements are denoted as *scanning* directions in the following.

In addition, measurements pointing straight towards the water surface were taken at elevation angles of −45° and −60° with respect to the horizon and in azimuthal directions of −45° and −90° relative to the ship's heading. These measurements containing strong liquid water effects are denoted as *water-pointing* measurements in the following. The length of the light path under water (and subsequently also the penetration depth) is varying not only by the applied viewing angles, but also during the day as a consequence of the position of the sun or the cleanliness of the water. Thus, the measurement ensemble represents an average of optical effects in natural liquid water.

3.6 Clear water and white caps measurements

In every water-pointing viewing direction, a series (40 s integration time) of single spectra was recorded with very short exposure times of only 100 ms each. Due to the short exposure time, these single measurements can be regarded as spectral snapshots without temporal evolution. The scene observed by the instrument was either a clear

AMTD
7, 5027–5073, 2014

and undisturbed view into the water body, or it was covered by white caps that occured almost periodically (depending on the roughness of the sea) when waves slapped against the ship or collided with its bow wave. Because of the very short exposure time, the measurements could be assigned to either *clear (blue) water* or *white caps* (in different magnitudes). A color index CI was applied to characterise the dominating color in the observed scene and to distinguish between these two cases. Therefore, the average intensity in the 413–419 nm interval was divided by the average intensity in the interval of 548–554 nm. All spectra with CI > 2 were assigned to the clear (blue) water spectra and those of CI <= 1 were assigned to the white caps spectra.

In first approximation, the spectra of the white caps can be regarded as the reflection of the incoming light before penetrating the water (the water surface is thought to be covered by a white plane), i.e. the difference between white caps and undisturbed water measurements is in first order determined by the spectral effects of liquid water. If the white caps measurements are used as reference spectra I_0 and the clear water spectra are used as attenuated spectra I, the optical depth of liquid water effects can be calculated in terms of the Lambert–Beer law (Eq. 2) as $\ln\left(I/I_0\right)$, which is exemplarily plotted for one measurement from 14 October 2009 in Fig. 2 (brown line) in comparison to the liquid water absorption coefficient from Pope and Fry (1997). Note that the MAX-DOAS field measurements are observations of scattered light, i.e. the brown curve in Fig. 2 contains elastic and inelastic scattering effects. Nevertheless, the similarity to the water absorption is remarkable demonstrating that these measurements are well-suited to study the liquid water absorption spectrum. In addition, the brown line reveals leftover structures from Fraunhofer lines which are caused by inelastic VRS. Thus, these measurements can be used to retrieve experimental cross-sections of H_2O_{liq} as well as VRS.

AMTD
7, 5027–5073, 2014

4 Retrieval of experimental (correction) spectra

Different approaches were tested in order to retrieve (a) experimental cross-sections of liquid water and VRS or (b) correction spectra of existing literature cross-sections. Therefore, the I and I_0 spectra (clear water, resp. white caps) were used in DOAS fits and a polynomial was fitted to the optical depths $\ln(I/I_0)$ to account for instrumental and elastic scattering effects. No trace gases were included in the fits as the difference between I and I_0 is considered to be liquid water effects only. In addition, in Sects. 4.3 and 4.4 a liquid water absorption spectrum (H_2O_{liq}) from literature was used in order to retrieve a correction spectrum for it. This H_2O_{liq} spectrum had to be adapted to our DOAS fit requirements as described in Sect. 4.1. To ensure that atmospheric conditions are as constant as possible, for each measurement I always the closest-in-time reference measurement I_0 was selected. As a cut-off criterion, only measurements I were taken for which a reference spectrum I_0 exists within $\Delta\mathrm{SZA} < 2^\circ$ (SZA = sun zenith angle). Also, only spectra recorded at $\mathrm{SZAs} < 85^\circ$ were used. After applying the color index and these restrictions ≈ 5000 measurements remained and could be analyzed. In addition, even stronger restrictions were tested: the individual 100 ms measurements for each intergration time were averaged according to their color index. Then, all spectra I were rejected if no I_0 exists within a period of 1 min. While this reduces the number of observations (predominantly because of the averaging), the results were always the same as in the first case.

4.1 Preparation of the literature H_2O_{liq} spectrum

As our DOAS routine requires cross-sections in 0.1 nm spacing but the liquid water absorption coefficient from literature (Pope and Fry, 1997) is provided only in 2.5 nm resolution, an interpolation was needed to fill the gaps. A simple linear interpolation yields an absorption spectrum with sharp peaks at the position of the original spectral points which is unrealistic. As Pope and Fry (1997) state that the resolution of their spectrum is only ≈ 7 nm, before the interpolation a running mean over 3 adjacent

AMTD
7, 5027–5073, 2014

spectral points (i.e., 7.5 nm) was applied yielding a smoother spectrum. Then, a spline interpolation was used (yielding a smoother spectrum than a linear interpolation) to obtain the required 0.1 nm spectrum.

Note that these changes return a H_2O_{liq} spectrum that is slightly different from the original one. The correction spectra retrieved in Sect. 4.3 and 4.4 were calculated using this prepared H_2O_{liq} cross-section and therefore describe corrections with respect to it.

4.2 Simultaneous retrieval of VRS and H_2O_{liq}

First, it was tested to retrieve experimental cross-sections of VRS and H_2O_{liq} simultaneously from DOAS residuals using a Principal Component Analysis (PCA). In the respective DOAS fit, only a polynomial accounting for elastic scattering under water was included (i.e., no H_2O_{liq} and no VRS). Thus, the differential spectra of both, VRS as well as H_2O_{liq} remained in the residuals.

In general, the idea of a PCA is to find a coordinate system in which a data set (here: set of DOAS residuals) can be expressed more efficiently than in the old coordinates. This is achieved by retrieving orthogonal basis vectors that point into the directions of largest variance in the data (thus, residuals corresponding to different strengths of liquid water effects are needed, which is the case for the measurements used here as mentioned above). As a result, the first few basis vectors or principal components may describe the variance in the whole data set already sufficiently. In addition, the principal components might have the meaning of cross-sections of absorbers or effects that were excluded in the DOAS fit (but this is not necessarily the case).

Various DOAS fits differing in the spectral range and order of polynomial were tested and for each fit the respective residuals were analysed using a PCA. However, the PCA was unable to separate the effects of H_2O_{liq} and VRS from each other. In particular, the retrieved H_2O_{liq} spectrum (first principal component) that is only broad-banded consisted always of both broad-band structures as well as small-band Fraunhofer structures which are in reality caused by VRS alone. To conclude, H_2O_{liq} and VRS are not orthogonal effects, i.e. the PCA retrieves components which produce variance in the

AMTD
7, 5027–5073, 2014

DOAS residuals independently from each other (orthogonal), which is not the case for VRS and H_2O_{liq}. Both effects can be expected to produce larger spectral structures if the light path under water increases. As a result, the conclusion here is that both effects depend very similarly on the length of the underwater light path, which is obvious. However, it has important implications because it overcomes the need to independently determine both, VRS as well as H_2O_{liq}. Instead, one cross-section, for example VRS, can be improved in a way that it does not only describe the VRS effect, but compensates at the same time for insufficiencies of H_2O_{liq}.

4.3 Retrieval of VRS

Aiming at the retrieval of an experimental differential VRS cross-section that compensates at the same time for insufficiencies of H_2O_{liq}, the prepared literature cross-section of H_2O_{liq} (see Sect. 4.1) was included in a DOAS fit. The fit was performed in a spectral range from 408–502 nm covering the NO_2 fitting window discussed in Sect. 5. Apart from the literature H_2O_{liq} spectrum, only a 4th order polynomial accounting for instrumental effects and elastic scattering under water was applied. This DOAS fit was performed on all water-pointing measurements (−45° and −60° elevation angle) throughout the whole campaign. Afterwards, the DOAS residuals were averaged. The result is plotted in Fig. 4 (red line) in comparison to the VRS cross-section modelled by SCIATRAN (blue line) for ground-based geometry and prevailing conditions during TransBrom. For consistency, a 4th order polynomial was subtracted from the simulated SCIATRAN VRS spectrum yielding a differential cross-section.

The similarity between the experimental and modelled VRS spectra in Fig. 4 is obvious. Nevertheless, some differences are observed, predominantly in the broad-band structures that are larger in the simulated spectrum – most obviously the step around 460 nm. This has two possible reasons: (1) The smoother shape of the broad-band structures could be realistic and caused by the uncertainty of H_2O_{liq} which is potentially compensated for by the experimental VRS spectrum. (2) As the DOAS method is a least-squares fit, the polynomial and the liquid water absorption are arranged in

AMTD
7, 5027–5073, 2014

a way that reproduces the measured optical depth $\tau(\lambda)$ optimally. Thus, in the DOAS retrieval fit the broad-band structures of VRS are partly compensated for by the DOAS polynomial and the broad H_2O_{liq} spectrum. While the first reason is speculative, the second reason is for sure true to some extent.

In addition, in the retrieval fit of the experimental VRS spectrum, no intensity offset correction was applied since this compensates very efficiently for the small-band VRS structures (incompletely removed Fraunhofer lines) as explained in Sect. 3.2. As a result, no retrieval of VRS was possible when the straylight correction was included. This implies that the resulting VRS spectrum in Fig. 4 might also contain small-band structures which are not caused by VRS alone but by straylight (or the detector's dark current) that might have been present in the spectrometer.

4.4 The H_2O_{res} (correction) spectrum

As mentioned above, the observation that the applied straylight correction compensates for small-band Fraunhofer structures from VRS is consistent with previous findings by Vountas et al. (2003). Thus, if H_2O_{liq}, a (constant) intensity offset correction (σ_{offset}), and a polynomial are included in a DOAS retrieval fit, then only the broad-band VRS structures plus uncertainties of liquid water absorption remain in the fit residuals.

In order to investigate this approach, several DOAS fits differing in the fit range and order of polynomial have been performed. The detailed settings are summarized in Table 1. The resulting residuals have been averaged for each DOAS fit and are exemplarily shown in Fig. 5a. Obviously, average residuals corresponding to different DOAS fits reveal the same general structure, even if retrieved in another fitting window or corresponding to another DOAS polynomial, i.e. the observed residual pattern seems to be rather stable. For example, the step at ≈ 460 nm which is caused by VRS is clearly visible in all spectra. Small-band structures are suppressed in the average residuals as a consequence of the applied straylight correction. The blue (slightly thicker) line in Fig. 5a results from a retrieval fit corresponding to the MAX-DOAS NO_2 fit settings

AMTD
7, 5027–5073, 2014

(425–497 nm, 3rd order polynomial). In the following, this spectrum is called the H_2O_{res} spectrum.

As mentioned in Sect. 4.1, some processing was necessary for the liquid water absorption coefficient from Pope and Fry (1997) allowing its use in our DOAS routine. The difference between the modified cross-section and the original one (simply linearly interpolated to 0.1 nm spacing) is shown in Fig. 5b (magenta line). Obviously, the resulting structures are much smaller than the H_2O_{res} spectrum. The magenta line was scaled by a factor of 20 (red line) so that the last peak is of the same size as the H_2O_{res} spectrum (blue line). The two curves show almost no agreement and the correlation was calculated to ≈ 0.1. Consequently, the retrieved H_2O_{res} spectrum can be assumed not to result from the changes applied to the H_2O_{liq} spectrum but correcting for so far unaccounted spectral structures of natural liquid water and VRS. In this context, it was also verified that the H_2O_{res} spectrum is different from the (differential) structures of water constituents, e.g. chlorophyll.

The advantage of the H_2O_{res} spectrum is that it is free of possible straylight contributions (and other intensity offsets) causing small-band structures. In DOAS fits above water surfaces, the H_2O_{res} spectrum can be used to compensate simultaneously for both, the uncertainties of the applied liquid water cross-section (from literature) and the broad-band structures of VRS while the small-band VRS structures are compensated for by the DOAS straylight correction (which accounts at the same time for possible real straylight pollution in the measurements). Thus, using the H_2O_{res} spectrum overcomes the need to introduce a (simulated) VRS spectrum in the DOAS fit. Furthermore, the H_2O_{res} spectrum has no Fraunhofer line features. As the DOAS fit requires independent cross-sections to obtain a meaningful solution (see Sect. 3.1) and VRS, (atmospheric) Ring spectrum, and intensity offset correction (σ_{offset}) are largely similar as consisting mainly of Fraunhofer line features, the use of the H_2O_{res} spectrum instead of VRS helps the reliability of the DOAS fit.

AMTD
7, 5027–5073, 2014

5 Effects of the H_2O_{res} spectrum on the MAX-DOAS NO_2 Fit

Four different MAX-DOAS fits of tropospheric NO_2 were performed in order to investigate the effect of the retrieved H_2O_{res} spectrum in *real* NO_2 analysis. Fit1 is based on the MAX-DOAS NO_2 fit used during the NO_2 intercomparison campaign CINDI (Roscoe et al., 2010) as well as the satellite NO_2 fit used at the IUP-Bremen (Richter et al., 2011). It contains neither VRS nor liquid water absorption. Fit2 uses the same settings, but this time the H_2O_{liq} spectrum is included. In addition to H_2O_{liq}, Fit3 contains the H_2O_{res} spectrum retrieved in Sect. 4.4. Fit4 equals Fit3, but the H_2O_{res} spectrum is replaced by the SCIATRAN simulated VRS spectrum shown in Fig. 4. The detailed fit settings are summarized in Table 2.

In contrast to the previous retrieval fits that were performed on water pointing measurements (elevation angles of −45°, resp. −60°), the NO_2 evaluation fits here are performed on vertical scanning measurements (i.e., elevation angles between −3° and 30°) which are commonly used to retrieve tropospheric NO_2 slant columns as well as vertical profiles. To avoid contributions of stratospheric NO_2 in the measurements, always the closest-in-time zenith observation was used as reference spectrum I_0. If no zenith spectrum was available within ΔSZA = 2° around the measurement I, the respective measurement was rejected.

For measurements in −3° elevation angle the H_2O_{liq} slant columns (or fit factors) of Fit2 are plotted in Fig. 6a in blue for the example of 14 October 2009, which was the day of best weather and viewing conditions and also clearest water during TransBrom. A clear diurnal shape is found, which is mainly the result of the position of the sun. Obviously, average underwater light paths of > 20 m occur around noon although only slightly pointing towards the sea surface. In addition to the H_2O_{liq} slant columns of Fit2, the (absolute values of) H_2O_{res} slant columns of Fit3 as well as the (absolute values of) VRS slant columns of Fit4 are plotted in Fig. 6a in red and green, respectively. The latter two lines have been scaled to the blue line in order to match into the figure according to

AMTD
7, 5027–5073, 2014

$$a_1 = \frac{(y_1, y_2)}{(y_2, y_2)} \quad a_2 = \frac{(y_1, y_3)}{(y_3, y_3)} \tag{5}$$

where $(\cdot)$ is the inner product, a_1, a_2 are the scaling factors for the red and green line and y_1, y_2, y_3 are the slant columns of H_2O_{liq}, H_2O_{res} and VRS, respectively.

Obviously, the diurnal shape of H_2O_{liq} slant columns in Fig. 6a is reproduced by the H_2O_{res} slant columns of Fit3 as well as the VRS slant columns of Fit4 indicating that all spectra describe effects that scale very similarly with the length of the light path under water. This was already concluded in Sect. 4.2 and it is the prerequisite for using the H_2O_{res} spectrum to account for both, broad-band strutures of VRS as well as uncertainties of liquid water absorption simultaneously.

In Fig. 6b the corresponding RMS of the fits shown in Fig. 6a are plotted in the same color coding. Apparently, the RMS of Fit2 is dominated by some water-related effects that are missing in the fit as the RMS reproduces the diurnal cycle of H_2O_{liq} slant columns in Fig. 6a (note that the H_2O_{liq} cross-section from literature is already included in Fit2). The RMS of Fit1 (no H_2O_{liq}) is outside the range of the figure and therefore not displayed, but it reproduces again the same shape. If the SCIATRAN simulated VRS cross-section is included in addition to H_2O_{liq} (Fit4, green line), the RMS is considerably smaller than in Fit2 (by up to a factor of 2 around noon). However, the same diurnal cycle is present in the RMS meaning that still some water-related optical depth is not accounted for. Finally, if the SCIATRAN VRS cross-section is replaced by the H_2O_{res} spectrum (Fit3, red line), absolute values decrease again by a factor of up to 2 around noon and – even more important – the diurnal shape of liquid water absorption is no longer present. This indicates that in Fit3 all water-related effects are compensated for – at least those which scale with the light path under water and which are detectable with our instrument (this is the objective of this study). To conclude, the H_2O_{res} spectrum works as intended and compensates (together with the straylight correction) for VRS as well as uncertainties of the applied liquid water absorption cross-section from literature.

AMTD
7, 5027–5073, 2014

Figure 7 shows the effect of the H_2O_{res} spectrum on the retrieved NO_2 slant columns. The TransBrom campaign encountered marine polluted regions of enhanced NO_2 as well as very clean open ocean regions of (almost) no NO_2 (Peters et al., 2012). Figures 7a and b are correlation plots between NO_2 slant columns from Fit2 vs. Fit1, and Fit3 vs. Fit1, respectively. In these plots, all measurements in the vertical scanning directions from the whole campaign are plotted using color coding: measurements at elevation angles from -3° to -1°, i.e. slightly towards the water surface, are displayed in red, 0° and 1° in green, and 2° to 30° in blue. Figure 7c and d are correlation plots of the corresponding RMS values of the different fits (same color-coding).

Only measurements taken under appropriate wind directions were used for fits 1 to 4, i.e. measurements were rejected if the wind direction would blow the ship's plume into the line of sight. This is true for both, the measurements I as well as the reference measurements I_0 meaning that the reference I_0 should not contain more NO_2 than the spectrum I. Thus, only positive NO_2 slant columns should be retrieved from the DOAS fits while negative slant columns indicate some problem in the fit (the fit would use the NO_2 cross-section to compensate for some other effect). In Fig. 7a, comparing the NO_2 slant columns retrieved from the basic NO_2 Fit1 and those from Fit2, two different cases have to be distinguished: (1) All positive NO_2 slant columns are located close to the 1 : 1 line, independently of the elevation angle of the respective measurement. Consequently, if NO_2 is present in the measurement, it is found correctly even if no liquid water absorption cross-section is included but the measurements certainly contain liquid water structures because slightly pointing towards the water surface (red data points are at the 1 : 1 line for positive NO_2 values). On the other hand, if (almost) no liquid water structures are present in the measurements but the H_2O_{liq} cross-section is included, this does not affect the retrieved NO_2 slant columns (blue data points are also on the 1 : 1 line), i.e. no mismatch of NO_2 is introduced by including H_2O_{liq} if this effect is not present in reality. (2) If NO_2 is not present in the measurement, it is still retrieved by Fit1, but in negative amounts. For -3° to -1° elevation angle, negative NO_2 slant columns of up to -1.5×10^{16} molec cm^{-2} are retrieved by Fit1 while measurements

AMTD
7, 5027–5073, 2014

above the horizon reach only $\approx -4 \times 10^{15}$ molec cm^{-2} (green and blue data points in inset). Thus, the larger the measurement's contamination with liquid water structures is, the larger the introduced error in NO_2 is. If the H_2O_{liq} cross-section is included (Fit2), the NO_2 is closer to zero and slant columns are only retrieved in negative amounts up to -2×10^{15} molec cm^{-2} (which is already in the range of the detection limit that was estimated in Peters et al., 2012, to 2×10^{-15} molec cm^{-2}), i.e. the problem is reduced but still present.

Using the H_2O_{res} spectrum overcomes this problem, as Fig. 7b demonstrates. In Fit3 containing not only liquid water absorption but also the H_2O_{res} spectrum, the negative offset in NO_2 for measurements containing no NO_2 but spectral effects of liquid water is no longer present (see inset of Fig. 7b: the red values scatter around zero within the DL of 2×10^{15} molec cm^{-2}). It is worth mentioning that this is not only the case for measurements towards the water (red data points), but also for measurements slightly above the horizon (green data points) implying that these measurements contain photons which have been partly under water before being (multiply) scattered into the instrument's line of sight. These directions provide the longest light path through the boundary layer and therefore highest sensitivity for tropospheric NO_2. Thus, the achieved improvement is important for the reliability of measurements especially of low NO_2 concentrations above the ocean.

All positive NO_2 slant columns in Fig. 7b are close to the 1 : 1 line, i.e. if NO_2 is present in the measurements the use of the H_2O_{res} spectrum does not affect the retrieved slant columns. This is consistent to the findings for H_2O_{liq} in Fig. 7a and the conclusion is that both, H_2O_{liq} as well as H_2O_{res} can be used in the MAX-DOAS NO_2 fit presented here without unintended side-effects but increasing the reliability of retrieved NO_2 slant columns over water.

Figure 7c and d demonstrate that the RMS of Fit2 and Fit3 is smaller than in Fit1. This is true for all elevation angles, but especially for those pointing slightly towards the water (red data points). Obviously, using the H_2O_{res} spectrum (Fit3) produces much smaller RMS than using liquid water absorption only (Fit2). Interestingly, the RMS of

AMTD
7, 5027–5073, 2014

Fit3 (Fig. 7d) is highest in 0° and 1° elevation angles (green data points). This is because the dominating effect on the RMS is no longer errors introduced by liquid water effects but misfits of water vapour in the atmosphere, which was present in large amounts in the humid air above the open ocean and for which largest slant columns occur in 0° and 1° elevation angles.

In order to quantify the improvement of the fit quality, the RMS of the different fits were compared to each other. Therefore, first, for each single measurement the difference of the RMS in two fits was calculated and normalized by the RMS of the first fit, e.g. (Fit1-Fit2)/Fit1 gives the relative improvement of Fit2 with respect to Fit1. Afterwards, the obtained values of single measurements were averaged in certain ranges of elevation angles (−3° to −1°, 0° and 1°, 2° to 30°). The results are summarized in Table 3 supporting the findings above. The largest RMS reduction is obtained by Fit3 with respect to Fit1 in the range of −3° to −1° which is on average ≈ 52.5 %, i.e. a factor of 2. For the same range of elevation angles, the comparison between Fit3 and Fit2 yields a RMS reduction of up to 30 % that is achieved by using the H_2O_{res} spectrum. In general, for all ranges of elevation angles the RMS reduction using the simulated VRS spectrum (Fit4) instead of the H_2O_{res} spectrum is smaller. Fit3 and Fit4 were directly compared yielding on average a better performance of Fit3 of 11.7 % in −3° to −1°, 4.1 % in 0° and 1°, and 3.2 % in 2° to 30°. Obviously, the improvement using the H_2O_{res} spectrum instead of the simulated VRS spectrum is larger in viewing directions containing more liquid water structures which is reasonable since the H_2O_{res} spectrum compensates for insufficiencies of H_2O_{liq}.

Finally, it has to be mentioned that the numbers in Table 3 are averages of a specific campaign encountering specific conditions (e.g., if more measurements in regions of very clean water had been performed, the value of (Fit1-Fit3)/Fit1 would have been even larger than it is here). Thus, the exact numbers do not necessarily apply to other measurements (under other conditions), but might represent typical values that can be expected for ship-based MAX-DOAS measurements over the ocean.

AMTD
7, 5027–5073, 2014

6 The H_2O_{res} spectrum in satellite data

In addition to MAX-DOAS data, the retrieved H_2O_{res} spectrum was also tested on OMI satellite data (see Sect. 3.3). Therefore, the four MAX-DOAS NO_2 fits from Sect. 5 from 425–497 nm (Table 3) have been adapted to satellite requirements. In particular, for OMI-Fit4 a VRS cross-section has been simulated with SCIATRAN using the satellite's nadir measurement geometry. The DOAS fits have been performed on OMI data for August 2007, i.e. for a different period than the TransBrom campaign. The fit details are summarized in Table 4.

Figure 8a shows the resulting slant columns of the H_2O_{res} spectrum in OMI-Fit3 (multiplied by −1 for better visualisation). Obviously, locations at which the H_2O_{res} structure is found coincide with the pattern of liquid water absorption (compare to Fig. 1 showing the H_2O_{liq} slant columns from OMI-Fit2), i.e. the H_2O_{res} spectrum is successfully found in measurements of a different instrument on a different platform using data from a different period. This demonstrates again that the H_2O_{res} spectrum is describing real liquid water residual effects and is not due to any MAX-DOAS instrumental effect.

Interestingly, the (broad-banded) H_2O_{res} spectrum is not only found over the ocean, but also over large desert regions in northern Africa and the Arabian peninsula (this is not visible in Fig. 8a as continents are masked out). The reason is most likely interference with broad-band sand structures which have been already found in GOME-2 data by Richter et al. (2011) over the desert.

In Fig. 8b the improvement of the RMS of OMI-Fit3, i.e. using the H_2O_{res} spectrum, with respect to OMI-Fit4 (simulated VRS instead H_2O_{res}) is shown. Therefore, the differences between the RMS of OMI-Fit4 and OMI-Fit3 have been calculated and normalized by the RMS of OMI-Fit4 (similar to Sect. 5). Obviously, at locations where the H_2O_{res} spectrum is found the RMS is decreased by up to ≈ 6 %. In the same way, the changes in RMS between the other fits were calculated and maximum values that occur over the ocean are summarized in Table 5. Including liquid water absorption leads to ≈ 45 % smaller RMS over the ocean (comparing OMI-Fit2 to OMI-Fit1). Taking into

AMTD
7, 5027–5073, 2014

account also VRS either by including a simulated VRS cross-section (OMI-Fit4) or the H_2O_{res} spectrum (OMI-Fit3) reduces the RMS with respect to OMI-Fit2 by up to ≈ 12 %, and ≈ 18 %, respectively. The H_2O_{res} spectrum performs up to ≈ 6 % better than the simluated VRS cross-section. Again, this is most likely because the H_2O_{res} spectrum is compensating not only broad-banded VRS structures, but also residual H_2O_{liq} structures which the simulated VRS spectrum is not doing. In general, maximum improvement is observed at locations of clearest water (compare Fig. 8b to Fig. 1) indicating that shorter light paths under water lead to smaller problems in the satellite data.

7 Summary and conclusions

Liquid water interacts with incident (solar) radiation in the Visible range in terms of absorption (H_2O_{liq}) and scattering (VRS, Brillouin) which has an impact on scattered light measured above the ocean (e.g., Fig. 1). While Brillouin scattering can be neglected for current DOAS instrument resolutions, the effects of liquid water absorption and VRS need to be compensated for in DOAS retrievals. This is not fully achieved using currently available cross-sections of H_2O_{liq} and VRS (Fig. 6).

In order to investigate liquid water effects, MAX-DOAS measurements pointing directly into very clear natural waters were taken during the TransBrom field campaign across the western Pacific in October 2009. Based on these measurements, it was not possible to retrieve independent experimental spectra of H_2O_{liq} and VRS because both effects depend in a similar way on the underwater light path (Fig. 6a). However, it turned out to be possible to apply a simultaneous correction to both effects by using only one correction spectrum. In addition, the intensity offset or straylight correction, which is routinely included in the DOAS analysis as an additional pseudo-absorber (Sect. 3.2), was found to compensate very efficiently for small-banded (incompletely removed Fraunhofer) structures produced by VRS. Thus, only the broad-band VRS structures need to be compensated for.

AMTD
7, 5027–5073, 2014

From experimental MAX-DOAS measurements we retrieved a residual correction spectrum (H_2O_{res}) comprising uncertainties of H_2O_{liq} as well as differential broad-band structures of VRS. Using the H_2O_{res} spectrum together with H_2O_{liq} in the MAX-DOAS NO_2 fit compensates entirely for liquid water absorption as well as VRS (Fig. 6b). In unpolluted marine environments where unrealistic negative NO_2 slant columns are retrieved in a standard evaluation, inclusion of the H_2O_{res} spectrum yields reasonable NO_2 slant columns scattering around zero within the detection limit (Fig. 7). On the other hand, the H_2O_{res} spectrum was found to have no effect on NO_2 slant columns in measurements containing no liquid water effects, i.e. no unwanted side-effects arise. At the same time, the RMS decreased by up to 30 % (depending on the elevation angle). Compared to a simulated VRS spectrum the H_2O_{res} spectrum performed up to ≈ 12 % better (Table 3). It is worth mentioning that this is most likely not because the retrieved H_2O_{res} spectrum is better than the SCIATRAN simulation of VRS, but because it accounts in addition for uncertainties of H_2O_{liq}.

The H_2O_{res} spectrum was tested in OMI satellite data over the ocean and was successfully found meaning that a potential improvement of satellite retrievals by our method is realistic (but not the topic of the present study). Maximum improvements of the DOAS fit quality due to the H_2O_{res} spectrum were found to be ≈ 18 % and it performs up to ≈ 6 % better than using a simulated VRS spectrum instead (Table 5).

To conclude, with the method presented in this study a complete compensation of all liquid water effects (absorption and VRS) was achieved in the MAX-DOAS analysis over the ocean. As our H_2O_{res} spectrum replaces the VRS spectrum, no radiative transfer modelling of VRS is necessary and the number of degrees of freedom of the DOAS fit stays constant (no additional cross-section is included). The retrieved H_2O_{res} spectrum can be used in other DOAS applications having similar settings (spectral range, order of polynomial) and using the same H_2O_{liq} cross-section as our retrieval fit.

Acknowledgements. We acknowledge the GEOMAR in Kiel, Germany, especially *Birgit Quack* and *Kirstin Krüger* for organizing the TransBrom campaign as well as the crew of the Research vessel *Sonne*. Tilman Dinter from IUP-Bremen provided VRS spectra simulated by SCIATRAN.

AMTD
7, 5027–5073, 2014

The ship measurements work for this paper was partly funded by the BMBF through grant 03G0731A. The contribution at TransBrom from University of Bremen was supported by the EU via the GEOMon Integrated Project (contract FP6-2005-Global-4-036677). The Bremen instrument was partly funded by the University of Bremen and the ENVIVAL-life project (50EE0839).

References

Bogumil, K., Orphal, J., Homann, T., Voigt, S., Spietz, P., Fleischmann, O. C., Vogel, A., Hartmann, M., Kromminga, H., Bovensmann, H., Frerick, J., and Burrows, J. P.: Measurements of molecular absorption spectra with the SCIAMACHY pre-flight model: instrument characterization and reference data for atmospheric remote-sensing in the 230–2380 nm region, J. Photochem. Photobiol. A, 157, 167–184, 2003. 5062

Bovensmann, H., Burrows, J. P., Buchwitz, M., Frerick, J., Noël, S., Rozanov, V. V., Chance, K. V., and Goede, A. P. H.: SCIAMACHY: mission objectives and measurement modes, J. Atmos. Sci., 56, 127–150, 1999. 5029

Bracher, A., Vountas, M., Dinter, T., Burrows, J. P., Röttgers, R., and Peeken, I.: Quantitative observation of cyanobacteria and diatoms from space using PhytoDOAS on SCIAMACHY data, Biogeosciences, 6, 751–764, doi:10.5194/bg-6-751-2009, 2009. 5030

Braun, C. L. and Smirnov, S. N.: Why is water blue?, J. Chem. Educ., 70, 612–614, 1993. 5033

Burrows, J. P., Hölzle, E., Goede, A. P. H., Visser, H., and Fricke, W.: SCIAMACHY – Scanning Imaging Absorption Spectrometer for Atmospheric Chartography, Acta Astronaut., 35, 445–451, 1995. 5029

Burrows, J. P., Weber, M., Buchwitz, M., Rozanov, V., Ladstatter-Weissenmayer, A., Richter, A., DeBeek, R., Hoogen, R., Bramstedt, K., Eichmann, K. U., and Eisinger, M.: The global ozone monitoring experiment (GOME): mission concept and first scientific results, J. Atmos. Sci., 56, 151–175, 1999. 5029

Burrows, J. P., Platt, U., and Borrell, P.: The Remote Sensing of Tropospheric Composition from Space, Physics of Earth and Space Environments, Springer, Berlin, Heidelberg, 2011. 5029

Callies, J., Corpaccioli, E., Eisinger, M., Hahne, A., and Lefebvre, A.: GOME-2 – Metop's Second-Generation Sensor for Operational Ozone Monitoring, ESA Bull.-Eur. Space, 102, 28–36, 2000. 5029

AMTD
7, 5027–5073, 2014

Chance, K. V. and Spurr, R. J. D.: Ring effect studies: Rayleigh scattering, including molecular parameters for rotational Raman scattering, and the Fraunhofer spectrum, Appl. Optics, 36, 5224–5230, 1997. 5062

De Smedt, I., Müller, J.-F., Stavrakou, T., van der A, R., Eskes, H., and Van Roozendael, M.: Twelve years of global observations of formaldehyde in the troposphere using GOME and SCIAMACHY sensors, Atmos. Chem. Phys., 8, 4947–4963, doi:10.5194/acp-8-4947-2008, 2008. 5029

Dickey, T. D., Kattawar, G. W., and Voss, K. J.: Shedding new light on light in the ocean, Phys. Today, 64, 44–49, 2011. 5031, 5035

Dinter, T., Rozanov, V. V., Burrows, J. P., and Bracher, A.: Retrieving the availability of light in the ocean utilising spectral signatures of Vibrational Raman Scattering in hyper-spectral satellite measurements, Appl. Optics, in preparation, 2014. 5030

Grainger, J. F. and Ring, J.: Anomalous Fraunhofer line profiles, Nature, 193, 762, doi:10.1038/193762a0, 1962. 5029, 5033

Großmann, K., Frieß, U., Peters, E., Wittrock, F., Lampel, J., Yilmaz, S., Tschritter, J., Sommariva, R., von Glasow, R., Quack, B., Krüger, K., Pfeilsticker, K., and Platt, U.: Iodine monoxide in the Western Pacific marine boundary layer, Atmos. Chem. Phys., 13, 3363–3378, doi:10.5194/acp-13-3363-2013, 2013. 5029, 5030, 5039

Heckel, A., Richter, A., Tarsu, T., Wittrock, F., Hak, C., Pundt, I., Junkermann, W., and Burrows, J. P.: MAX-DOAS measurements of formaldehyde in the Po-Valley, Atmos. Chem. Phys., 5, 909–918, doi:10.5194/acp-5-909-2005, 2005. 5029

Hickman, G. D., Harding, J. M., Carnes, M., Pressman, A., Kattawar, G. W., and Fry, E. S.: Aircraft laser sensing of sound-velocity in water – Brillouin-scattering, Remote Sens. Environ., 36, 165–178, 1991. 5035

Joiner, J., Vasilkov, A. P., Flittner, D. E., Gleason, J. F., and Bhartia, P. K.: Retrieval of cloud pressure and oceanic chlorophyll content using Raman scattering in GOME ultraviolet spectra, J. Geophys. Res.-Atmos., 109, D01109, doi:10.1029/2003jd003698, 2004. 5030

Kattawar, G. W. and Xu, X.: Filling in of Fraunhofer lines in the ocean by Raman-scattering, Appl. Optics, 31, 6491–6500, 1992. 5029, 5034, 5068

Kattawar, G. W., Young, A. T., and Humphreys, T. J.: Inelastic scattering in planetary atmospheres. I. The Ring effect, without aerosols, The Astrophysical Journal, 243, 1049–1057, 1981. 5033

AMTD
7, 5027–5073, 2014

Krüger, K. and Quack, B.: Introduction to special issue: the *TransBrom Sonne* expedition in the tropical West Pacific, Atmos. Chem. Phys., 13, 9439–9446, doi:10.5194/acp-13-9439-2013, 2013. 5039

Leonard, D. A., Caputo, B., and Hoge, F. E.: Remote-sensing of subsurface water temperature by Raman-scattering, Appl. Optics, 18, 1732–1745, 1979. 5034

Lerot, C., Stavrakou, T., De Smedt, I., Müller, J.-F., and Van Roozendael, M.: Glyoxal vertical columns from GOME-2 backscattered light measurements and comparisons with a global model, Atmos. Chem. Phys., 10, 12059–12072, doi:10.5194/acp-10-12059-2010, 2010. 5031

Levelt, P. F., Hilsenrath, E., Leppelmeier, G. W., van den Oord, G. H. J., Bhartia, P. K., Tamminen, J., de Haan, J. F., and Veefkind, J. P.: Science objectives of the Ozone Monitoring Instrument, IEEE T. Geosci. Remote, 44, 1199–1208, 2006a. 5029, 5039

Levelt, P. F., Van den Oord, G. H. J., Dobber, M. R., Malkki, A., Visser, H., de Vries, J., Stammes, P., Lundell, J. O. V., and Saari, H.: The Ozone Monitoring Instrument, IEEE T. Geosci. Remote, 44, 1093–1101, 2006b. 5029, 5039

Martin, R. V., Chance, K., Jacob, D. J., Kurosu, T. P., Spurr, R. J. D., Bucsela, E., Gleason, J. F., Palmer, P. I., Bey, I., Fiore, A. M., Li, Q. B., Yantosca, R. M., and Koelemeijer, R. B. A.: An improved retrieval of tropospheric nitrogen dioxide from GOME, J. Geophys. Res.-Atmos., 107, 4437, doi:10.1029/2001jd001027, 2002. 5029

Peters, E.: Improved MAX-DOAS Measurements and Retrievals Focused on the Marine Boundary Layer, Ph.D. thesis, University of Bremen, available at: http://elib.suub.uni-bremen.de/peid=D00103447 (last access: 20 May 2014), 2013. 5035

Peters, E., Wittrock, F., Großmann, K., Frieß, U., Richter, A., and Burrows, J. P.: Formaldehyde and nitrogen dioxide over the remote western Pacific Ocean: SCIAMACHY and GOME-2 validation using ship-based MAX-DOAS observations, Atmos. Chem. Phys., 12, 11179–11197, doi:10.5194/acp-12-11179-2012, 2012. 5029, 5039, 5049, 5050

Pinardi, G., Van Roozendael, M., Abuhassan, N., Adams, C., Cede, A., Clémer, K., Fayt, C., Frieß, U., Gil, M., Herman, J., Hermans, C., Hendrick, F., Irie, H., Merlaud, A., Navarro Comas, M., Peters, E., Piters, A. J. M., Puentedura, O., Richter, A., Schönhardt, A., Shaiganfar, R., Spinei, E., Strong, K., Takashima, H., Vrekoussis, M., Wagner, T., Wittrock, F., and Yilmaz, S.: MAX-DOAS formaldehyde slant column measurements during CINDI: intercomparison and analysis improvement, Atmos. Meas. Tech., 6, 167–185, doi:10.5194/amt-6-167-2013, 2013. 5029, 5039

AMTD
7, 5027–5073, 2014

Piters, A. J. M., Boersma, K. F., Kroon, M., Hains, J. C., Van Roozendael, M., Wittrock, F., Abuhassan, N., Adams, C., Akrami, M., Allaart, M. A. F., Apituley, A., Beirle, S., Bergwerff, J. B., Berkhout, A. J. C., Brunner, D., Cede, A., Chong, J., Clémer, K., Fayt, C., Frieß, U., Gast, L. F. L., Gil-Ojeda, M., Goutail, F., Graves, R., Griesfeller, A., Großmann, K., Hemerijckx, G., Hendrick, F., Henzing, B., Herman, J., Hermans, C., Hoexum, M., van der Hoff, G. R., Irie, H., Johnston, P. V., Kanaya, Y., Kim, Y. J., Klein Baltink, H., Kreher, K., de Leeuw, G., Leigh, R., Merlaud, A., Moerman, M. M., Monks, P. S., Mount, G. H., Navarro-Comas, M., Oetjen, H., Pazmino, A., Perez-Camacho, M., Peters, E., du Piesanie, A., Pinardi, G., Puentedura, O., Richter, A., Roscoe, H. K., Schönhardt, A., Schwarzenbach, B., Shaiganfar, R., Sluis, W., Spinei, E., Stolk, A. P., Strong, K., Swart, D. P. J., Takashima, H., Vlemmix, T., Vrekoussis, M., Wagner, T., Whyte, C., Wilson, K. M., Yela, M., Yilmaz, S., Zieger, P., and Zhou, Y.: The Cabauw Intercomparison campaign for Nitrogen Dioxide measuring Instruments (CINDI): design, execution, and early results, Atmos. Meas. Tech., 5, 457–485, doi:10.5194/amt-5-457-2012, 2012. 5039

Platt, U.: Differential optical absorption spectroscopy (DOAS), Chem. Anal. Series, 127, 27–83, 1994. 5029, 5035

Platt, U. and Stutz, J.: Differential Optical Absorption Spectroscopy: Principles and Applications, Physics of Earth and Space Environments, Springer, 2008. 5035

Pope, R. M. and Fry, E. S.: Absorption spectrum (380–700 nm) of pure water. II. Integrating cavity measurements, Appl. Optics, 36, 8710–8723, 1997. 5029, 5031, 5033, 5039, 5041, 5042, 5046, 5061, 5062, 5064, 5067, 5070

Quack, B.: Cruise Report TransBrom SONNE, Tech. rep., IFM Geomar, 2010. 5039

Richter, A., Burrows, J. P., Nüß, H., Granier, C., and Niemeier, U.: Increase in tropospheric nitrogen dioxide over China observed from space, Nature, 437, 129–132, 2005. 5029

Richter, A., Begoin, M., Hilboll, A., and Burrows, J. P.: An improved NO_2 retrieval for the GOME-2 satellite instrument, Atmos. Meas. Tech., 4, 1147–1159, doi:10.5194/amt-4-1147-2011, 2011. 5030, 5047, 5052

Roscoe, H. K., Van Roozendael, M., Fayt, C., du Piesanie, A., Abuhassan, N., Adams, C., Akrami, M., Cede, A., Chong, J., Clémer, K., Friess, U., Gil Ojeda, M., Goutail, F., Graves, R., Griesfeller, A., Grossmann, K., Hemerijckx, G., Hendrick, F., Herman, J., Hermans, C., Irie, H., Johnston, P. V., Kanaya, Y., Kreher, K., Leigh, R., Merlaud, A., Mount, G. H., Navarro, M., Oetjen, H., Pazmino, A., Perez-Camacho, M., Peters, E., Pinardi, G., Puentedura, O., Richter, A., Schönhardt, A., Shaiganfar, R., Spinei, E., Strong, K., Takashima, H.,

AMTD
7, 5027–5073, 2014

Vlemmix, T., Vrekoussis, M., Wagner, T., Wittrock, F., Yela, M., Yilmaz, S., Boersma, F., Hains, J., Kroon, M., Piters, A., and Kim, Y. J.: Intercomparison of slant column measurements of NO_2 and O_4 by MAX-DOAS and zenith-sky UV and visible spectrometers, Atmos. Meas. Tech., 3, 1629–1646, doi:10.5194/amt-3-1629-2010, 2010. 5039, 5047

Rothman, L. S., Barbe, A., Benner, D. C., Brown, L. R., Camy-Peyret, C., Carleer, M. R., Chance, K., Clerbaux, C., Dana, V., Devi, V. M., Fayt, A., Flaud, J. M., Gamache, R. R., Goldman, A., Jacquemart, D., Jucks, K. W., Lafferty, W. J., Mandin, J. Y., Massie, S. T., Nemtchinov, V., Newnham, D. A., Perrin, A., Rinsland, C. P., Schroeder, J., Smith, K. M., Smith, M. A. H., Tang, K., Toth, R. A., Vander Auwera, J., Varanasi, P., and Yoshino, K.: The HITRAN molecular spectroscopic database: edition of 2000 including updates through 2001, J. Quant. Spectrosc. Ra., 82, 5–44, 2003. 5062

Rozanov, V. V. and Vountas, M.: Radiative transfer equation accounting for rotational Raman scattering and its solution by the discrete-ordinates method, J. Quant. Spectrosc. Ra., 133, 603–618, 2014. 5036

Rozanov, V. V., Rozanov, A. V., Kokhanovsky, A. A., and Burrows, J. P.: Radiative transfer through terrestrial atmosphere and ocean: Software package SCIATRAN, J. Quant. Spectrosc. Ra., 133, 13–71, 2014. 5030, 5036, 5069

Schönhardt, A., Richter, A., Wittrock, F., Kirk, H., Oetjen, H., Roscoe, H. K., and Burrows, J. P.: Observations of iodine monoxide columns from satellite, Atmos. Chem. Phys., 8, 637–653, doi:10.5194/acp-8-637-2008, 2008. 5029

Schönhardt, A., Altube, P., Gerilowski, K., Krautwurst, S., Hartmann, J., Meier, A. C., Richter, A., and Burrows, J. P.: A wide field-of-view imaging DOAS instrument for continuous trace gas mapping from aircraft, Atmos. Meas. Tech. Discuss., 7, 3591–3644, doi:10.5194/amtd-7-3591-2014, 2014. 5029

Vandaele, A. C., Hermans, C., Simon, P. C., Roozendael, M. V., Guilmot, J. M., Carleer, M., and Colin, R.: Fourier transform measurement of NO_2 absorption cross-section in the visible range at room temperature, J. Atmos. Chem., 25, 289–305, 1996. 5062

Vandaele, A. C., Fayt, C., Hendrick, F., Hermans, C., Humbled, F., Van Roozendael, M., Gil, M., Navarro, M., Puentedura, O., Yela, M., Braathen, G., Stebel, K., Tornkvist, K., Johnston, P., Kreher, K., Goutail, F., Mieville, A., Pommereau, J. P., Khaikine, S., Richter, A., Oetjen, H., Wittrock, F., Bugarski, S., Friess, U., Pfeilsticker, K., Sinreich, R., Wagner, T., Corlett, G., and Leigh, R.: An intercomparison campaign of ground-based UV-visible measurements of

AMTD
7, 5027–5073, 2014

NO_2, BrO, and OClO slant columns: methods of analysis and results for NO_2, J. Geophys. Res.-Atmos., 110, D08305, doi:10.1029/2004jd005423, 2005. 5062

Vountas, M., Rozanov, V. V., and Burrows, J. P.: Ring effect: impact of rotational Raman scattering on radiative transfer in Earth's atmosphere, J. Quant. Spectrosc. Ra., 60, 943–961, 1998. 5036

Vountas, M., Richter, A., Wittrock, F., and Burrows, J. P.: Inelastic scattering in ocean water and its impact on trace gas retrievals from satellite data, Atmos. Chem. Phys., 3, 1365–1375, doi:10.5194/acp-3-1365-2003, 2003. 5030, 5038, 5045

Vountas, M., Dinter, T., Bracher, A., Burrows, J. P., and Sierk, B.: Spectral studies of ocean water with space-borne sensor SCIAMACHY using Differential Optical Absorption Spectroscopy (DOAS), Ocean Sci., 3, 429–440, doi:10.5194/os-3-429-2007, 2007. 5030

Walrafen, G. E.: Raman spectral studies of effects of temperature on water structure, J. Chem. Phys., 47, 114, doi:10.1063/1.1711834, 1967. 5034, 5068

Wittrock, F., Oetjen, H., Richter, A., Fietkau, S., Medeke, T., Rozanov, A., and Burrows, J. P.: MAX-DOAS measurements of atmospheric trace gases in Ny-Ålesund – Radiative transfer studies and their application, Atmos. Chem. Phys., 4, 955–966, doi:10.5194/acp-4-955-2004, 2004. 5029

Wittrock, F., Richter, A., Oetjen, H., Burrows, J. P., Kanakidou, M., Myriokefalitakis, S., Volkamer, R., Beirle, S., Platt, U., and Wagner, T.: Simultaneous global observations of glyoxal and formaldehyde from space, Geophys. Res. Lett., 33, L16804, doi:10.1029/2006gl026310, 2006. 5029

Xu, X. and Kattawar, G. W.: Filling in of Fraunhofer lines in the ocean by Brillouin-scattering, Appl. Optics, 33, 4835–4840, doi:10.1364/AO.33.004835, 1994. 5029, 5034, 5035

AMTD
7, 5027–5073, 2014

Table 1. Settings for the different H_2O_{res} retrieval fits.

Parameter	H_2O_{res} retrieval fit	Remarks
Elevation angle	−45°, −60°	and different azimuths
SZA	< 85°	
Measurements (I)	clear water	100 ms individual as well as integrated
Reference (I_0)	closest sea spray	ΔSZA ≤ 2°, Δt ≤ 1 min
Fitting window	408–502 nm, 412–498 nm, 412–470 nm 425–497 nm	 NO_2 fitting window
DOAS polynomial	2nd, 3rd, 4th order	3rd corresponds to NO_2 fit
Straylight correction	constant and linear	linear only tested (no further improvement observed)
Liquid water VRS	included not included	Pope and Fry (1997) SCIATRAN (Fig. 4)

AMTD
7, 5027–5073, 2014

Table 2. Settings for different NO_2 fits (with and without VRS, H_2O_{res} and H_2O_{liq}) performed to evaluate the effect of the retrieved H_2O_{res}-spectrum. The fits were performed on measurements pointing in elevation angles between −3° (slightly towards the water surface) and 30°.

Parameter	Fit1	Fit2	Fit3	Fit4	Remarks
H_2O_{liq}	No	Yes	Yes	Yes	prepared (Sect. 4.1) Pope and Fry (1997)
H_2O_{res}	No	No	Yes	No	Blue line in Fig. 5a, b
VRS (SCIATRAN)	No	No	No	Yes	Blue line in Fig. 4
Common Parameters					
O_3	223 K, (Bogumil et al., 2003)				same for all fits
NO_2	295 K, (Vandaele et al., 1996)				same for all fits
O_4	Hermans et al., unpublished (http://spectrolab.aeronomie.be/o2.htm)				same for all fits
Water vapour	Vandaele et al. (2005), Rothman et al. (2003) using HITRAN 2009				same for all fits
Ring	following (Chance and Spurr, 1997)				same for all fits
Polynomial	3rd order				same for all fits
Fit range	425–497 nm				same for all fits
Straylight correction	constant				same for all fits
Reference (I_0)	zenith direction, closest in time				same for all fits

AMTD
7, 5027–5073, 2014

Table 3. Normalized RMS differences (in %) of the performed fits averaged in specific ranges of elevation angles.

	−3°, −2°, −1°	0° and 1°	2° to 30°
(Fit1-Fit2)/Fit1	37.6	10.6	10.9
(Fit1-Fit3)/Fit1	52.5	20.0	18.0
(Fit1-Fit4)/Fit1	48.4	16.8	15.4
(Fit2-Fit3)/Fit2	29.7	11.1	8.5
(Fit4-Fit3)/Fit4	11.7	4.1	3.2

AMTD
7, 5027–5073, 2014

Table 4. Settings for the DOAS test fits on OMI data. The OMI-Fits correspond to the MAX-DOAS NO_2 fits from Table 2.

Parameter	OMI-Fit1	OMI-Fit2	OMI-Fit3	OMI-Fit4	Remarks
H_2O_{liq}	No	Yes	Yes	Yes	prepared (Sect. 4.1) Pope and Fry (1997)
H_2O_{res}	No	No	Yes	No	Blue line in Fig. 5a, b
VRS (SCIATRAN)	No	No	No	Yes	SCIATRAN simulation for satellite geometry
Common Parameters					
Trace gases	O_3(223 K), NO_2(295 K), O_4, water vapour, Ring				same for all fits
Polynomial	3rd order				same for all fits
Fit range	425–497 nm				same for all fits
Straylight correction	constant				same for all fits
Reference (I_0)	solar spectrum				same for all fits
Period	Aug 2007				same for all fits

AMTD
7, 5027–5073, 2014

Table 5. Normalized RMS differences (in %) of the performed OMI-fits (maximum values over the ocean). On a global scale, the RMS ratio (Fit4–Fit3)/Fit4 is plotted in Fig. 8b.

	(Fit1–Fit2)/Fit1	(Fit2–Fit3)/Fit2	(Fit2–Fit4)/Fit2	(Fit4 - Fit3)/Fit4
Max. over ocean	≈ 45 %	≈ 18 %	≈ 12 %	≈ 6 %

AMTD
7, 5027–5073, 2014

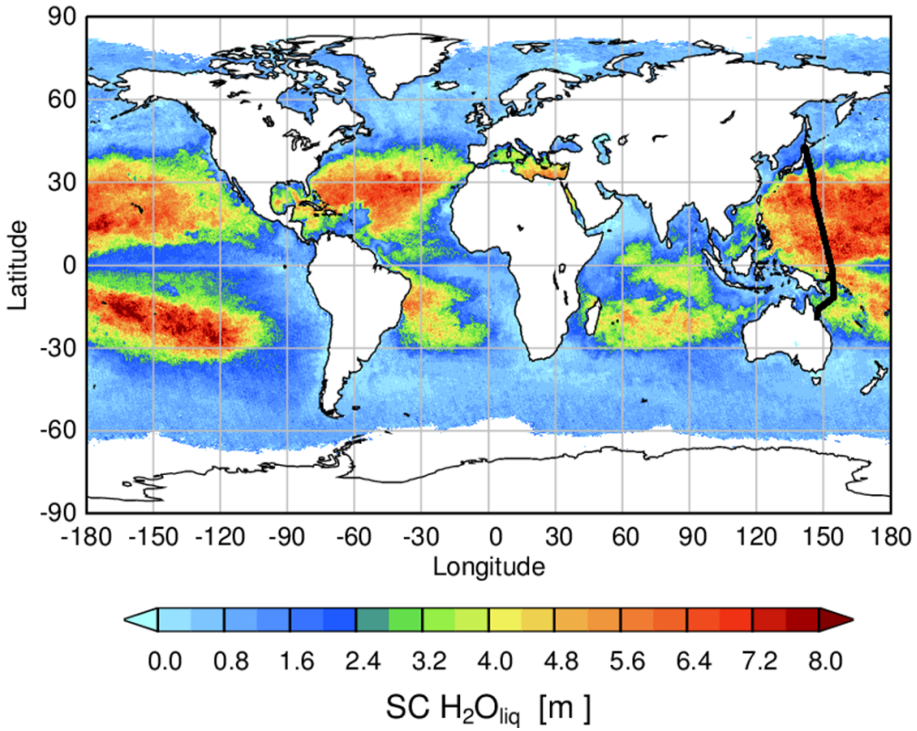

Figure 1. Liquid water absorption (average length of the light path under water) as observed from OMI for August 2007 using the DOAS technique (for fit details, see Sect. 6). The cruise track during TransBrom is indicated in black.

AMTD
7, 5027–5073, 2014

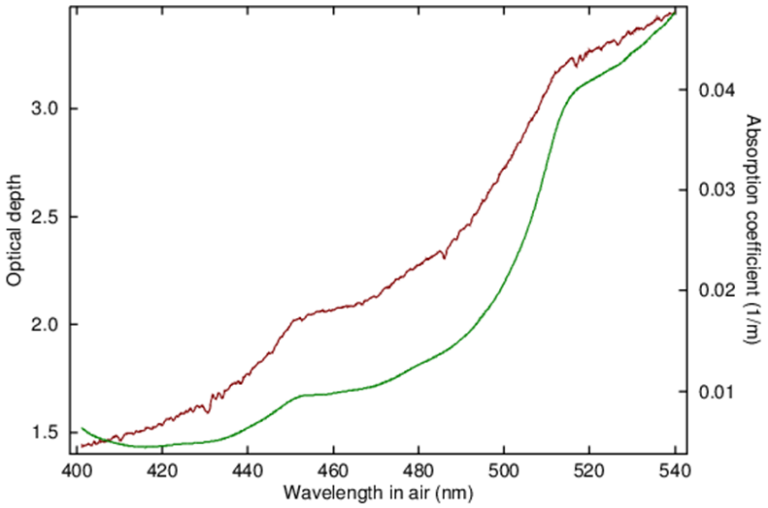

Figure 2. Green: liquid water absorption coefficient (H_2O_{liq} spectrum) from Pope and Fry (1997). Brown: logarithm of the ratio between an undisturbed and a white caps spectrum in water pointing direction as described in Sect. 3.6, i.e. optical depth of water (exemplarily for one measurement on 14 October 2009).

AMTD
7, 5027–5073, 2014

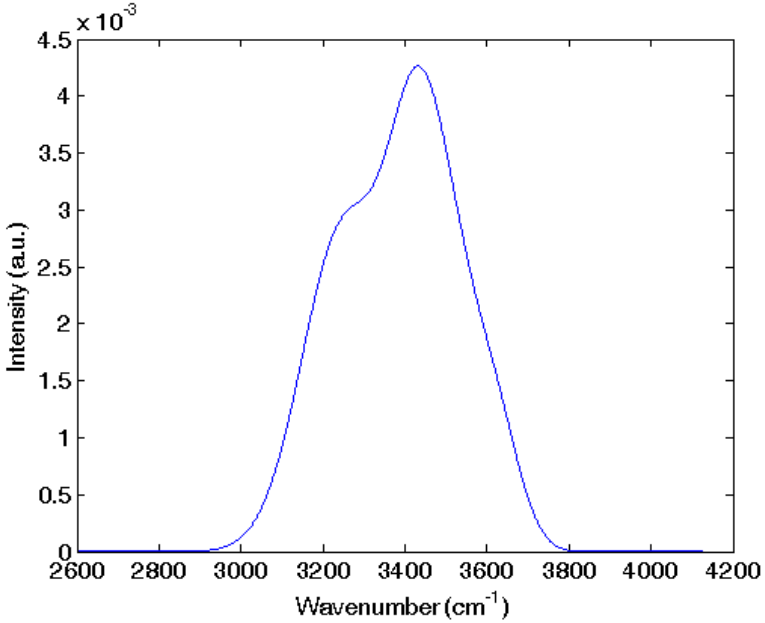

Figure 3. Illustration of the VRS band. The line shape was calculated according to Walrafen (1967) and Kattawar and Xu (1992).

AMTD
7, 5027–5073, 2014

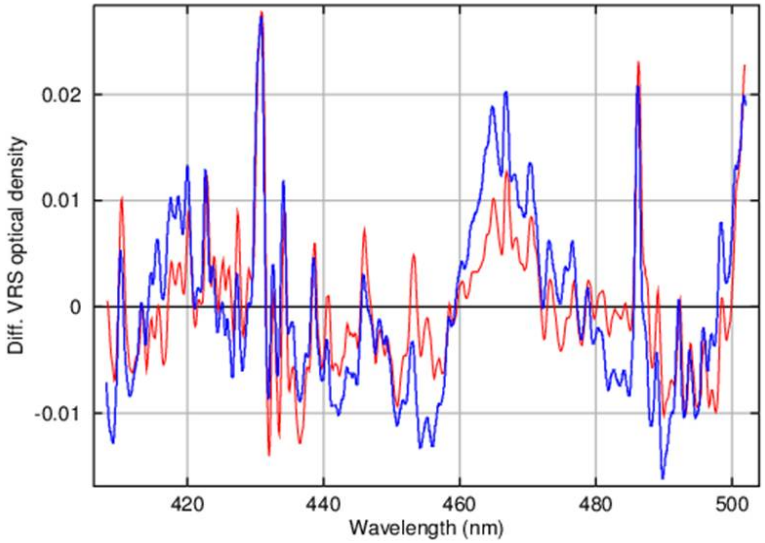

Figure 4. Blue: differential VRS cross-section simulated using SCIATRAN (Rozanov et al., 2014) for geometrical settings according to the ground-based measurements performed during TransBrom (V. Rozanov, personal communication, 2012). Red: diff. VRS cross-section retrieved from MAX-DOAS measurements (see Sect. 4).

AMTD
7, 5027–5073, 2014

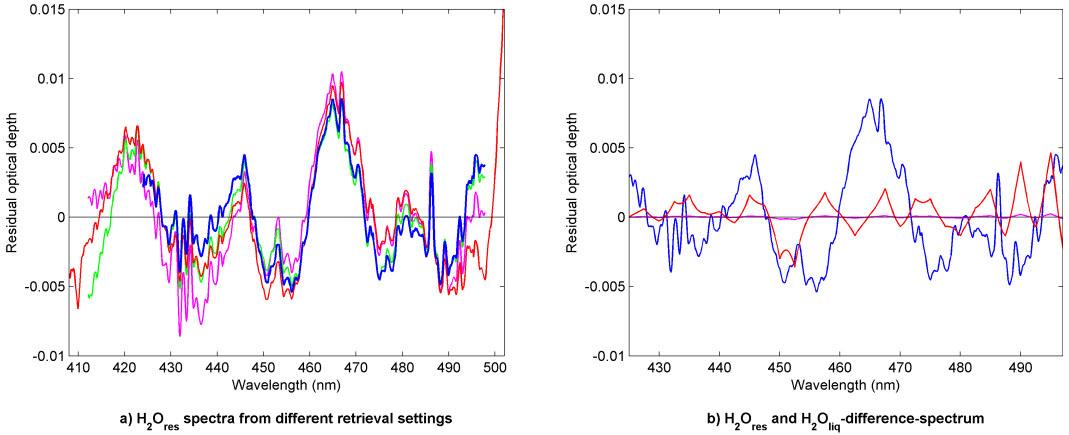

Figure 5. (a) Exemplary H_2O_{res} spectra obtained from different retrieval fit settings. Magenta: 412–498 nm and 2nd order polynomial, green: 412–498 nm and 4th order polynomial, red: 408–502 nm and 4th order polynomial, blue: 425–497 nm and 3rd order polynomial (= NO_2 fit range and polynomial). **(b)** H_2O_{res} spectrum from NO_2 fit settings in blue compared to the difference spectrum between applied H_2O_{liq} spectrum and (linear interpolated) spectrum from Pope and Fry (1997) in magenta (scaled by 20 in red).

AMTD
7, 5027–5073, 2014

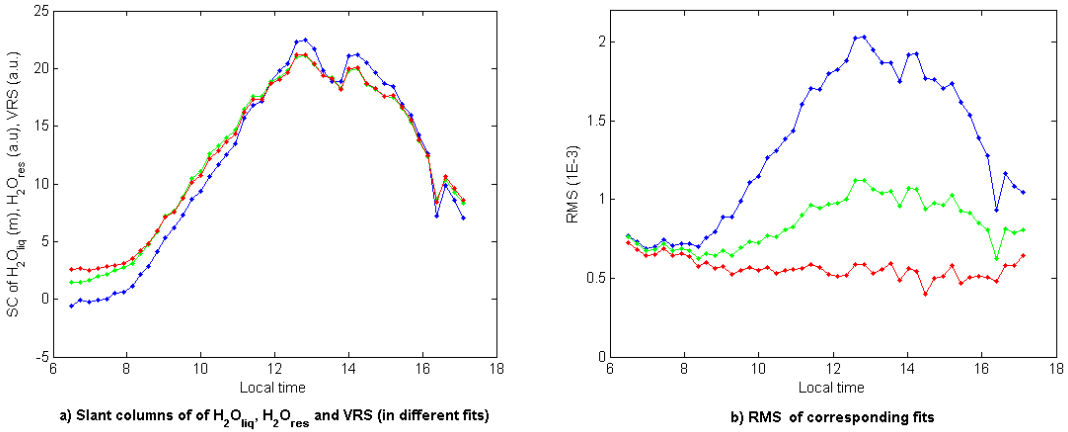

Figure 6. Fit results from measurements in −3° elevation on 14 October 2009: **(a)** H_2O_{liq}-SC of Fit2 in blue, H_2O_{res}-SC (absolute values) of Fit3 in red and VRS-SC (absolute values) of Fit4 in green (the red and green line were scaled to the blue line in order to match into the figure). **(b)** RMS of the corresponding Fits (Fit2 = blue, Fit3 = red, Fit4 = green). For fit parameters, see Table 2.

AMTD
7, 5027–5073, 2014

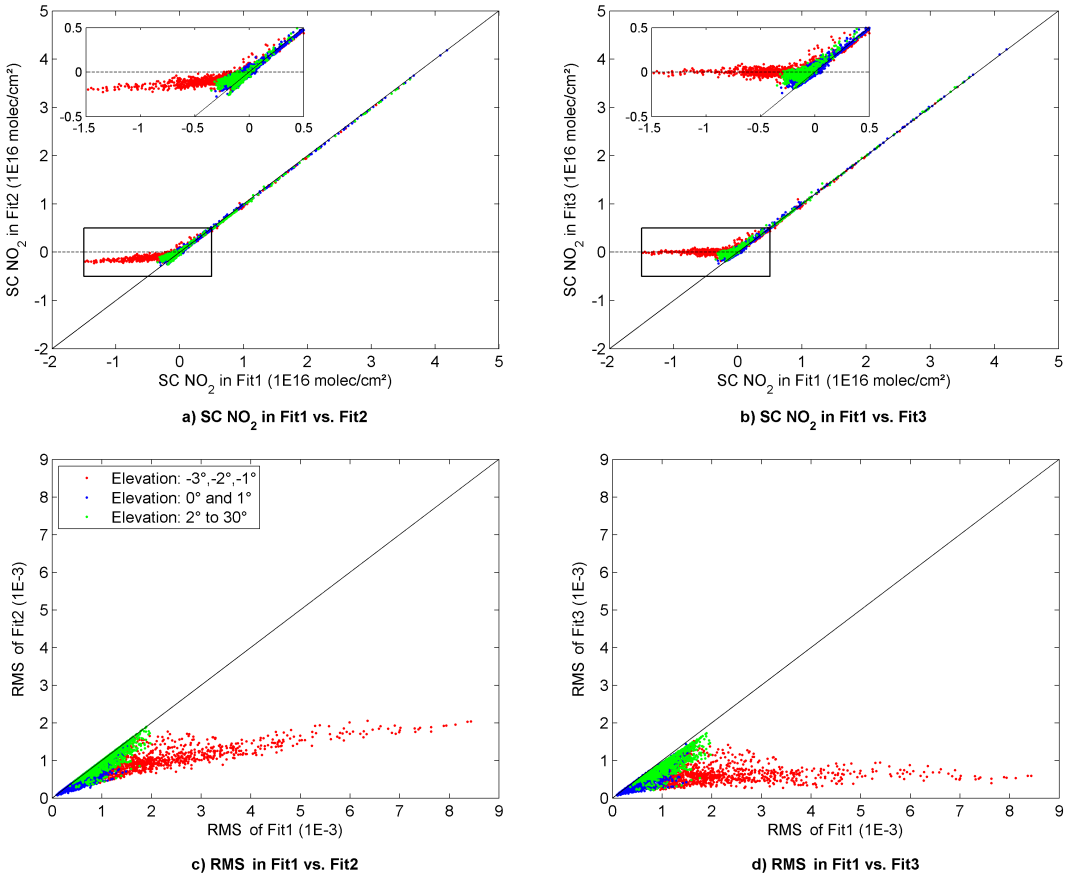

Figure 7. Influence of the H_2O_{res}-spectrum on the NO_2 slant column and RMS in different DOAS fits.

AMTD
7, 5027–5073, 2014

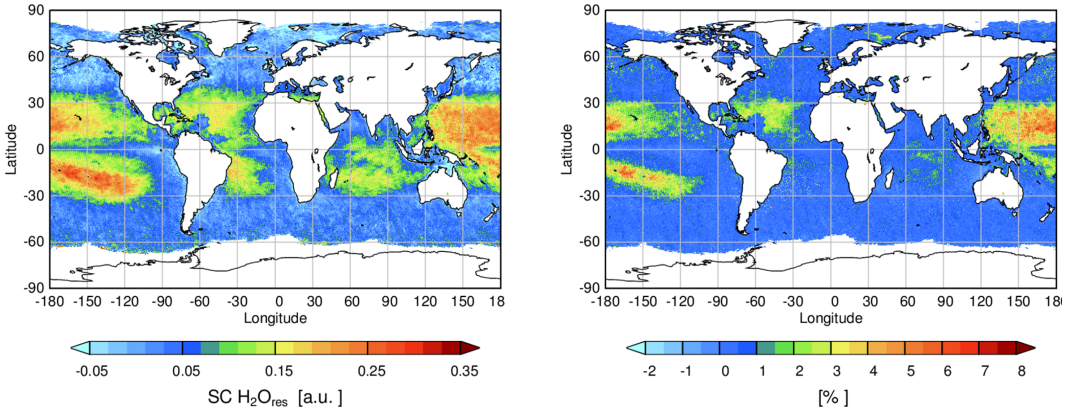

(a) OMI-Fit3: H_2O_{res} slant columns

(b) OMI RMS: (Fit4 - Fit3)/Fit4

Figure 8. (a) H_2O_{res} slant columns of OMI-Fit3. **(b)** Normalized difference between the RMS in OMI-Fit4 and OMI-Fit3, i.e. RMS (Fit4–Fit3)/Fit4, in percent. For fit settings, see Table 4.

AMTD
7, 5027–5073, 2014